Supplementary Information

Nanotextured Superhydrophobic Electrodes enable Detection of attomolar-scale DNA concentration within a Droplet by non-Faradaic Impedance Spectroscopy

Aida Ebrahimi[a,b], Piyush Dak[a,b], Eric Salm[d,e], Susmita Dash[b,c], Suresh V. Garimella[b,c], Rashid Bashir[d,e,f], and Muhammad A. Alam[a,b,]*

[a] *School of Electrical and Computer Engineering, Purdue University, West Lafayette, IN 47907, USA*

[b] *Birck Nanotechnology Center, Purdue University, West Lafayette, IN 47907, USA*

[c] *School of Mechanical Engineering, Purdue University, West Lafayette, IN 47907, USA*

[d] *Department of Bioengineering, University of Illinois at Urbana-Champaign, Urbana, IL 61801, USA*

[e] *Micro and Nanotechnology Lab, University of Illinois at Urbana-Champaign, Urbana, IL 61801, USA*

[f] *Department of Electrical and Computer Engineering, University of Illinois at Urbana-Champaign, Urbana-Champaign, IL 61801, USA*

* Corresponding author: alam@purdue.edu, Phone: (765) 494-5988

S1 Design of the Multifunctional Superhydrophobic Electrodes

Design and fabrication of textured hydrophobic surfaces has attracted a lot of attention in the past few years for application in many research fields, including biosensors and microelectronics [1,2]. Droplet evaporation on these surfaces has been comprehensively studied by He *et al.* [2] and McHale *et al.* [3]

The shape of a sessile droplet on a surface depends on the surface material, and its roughness, the ambient temperature, and the manner by which the droplet is deposited [4]. On a textured surface, the droplet can assume two different shapes with corresponding contact angles that follow one of the following modes:

(i)   In the Cassie-Baxter mode which is schematically shown in Fig. S1.1 (a), the droplet sits on top of the underlying structural features, trapping air pockets within the structure [2,3,5]. In this state, the contact angle of the droplet approximately follows the Cassie-Baxter formula:

$$\cos\theta_{CB} = f_s\left(\cos\theta_e + 1\right) - 1, \qquad S1(1)$$

where f_s is the solid fraction of the roughness features [2].

(ii)   In the Wenzel mode shown in Fig. S1.1 (b), the droplet fills the structural features and completely wets the surface. The Wenzel formula for the contact angle is given by:

$$\cos\theta_W = r\cos\theta_e, \qquad S1(2)$$

where θ_W is the Wenzel contact angle, θ_e is the equilibrium contact angle of a drop on a smooth surface, and r is the surface roughness defined as the actual area of the rough surface divided by the projected area [2].
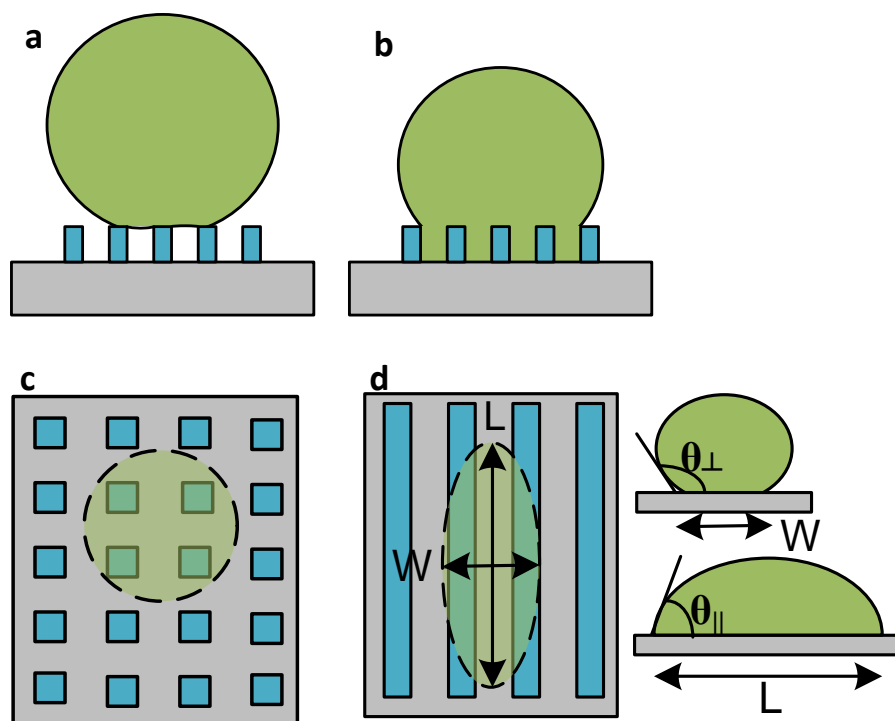
Fig. S1.1 Illustration of a droplet in (a) the Cassie state, in which the droplet does not fill the air gaps between the roughness elements, and in (b) the Wenzel state, in which the droplet completely penetrates the air gaps underneath. (c) The droplet forms a circular contact line on a symmetric surface and, (d) an oval-shaped contact line on an asymmetric surface. For asymmetric surfaces, the droplet faces energy barriers in the direction perpendicular to the ridges (blue rectangles) and is pinned, while it spreads in the direction parallel to the ridges. This results in droplet elongation, with different contact angles in the two directions.

In an attempt to mimic the "lotus effect" [6], most research on artificial hydrophobic structures has been focused on exploring the characteristics of droplets on symmetrically patterned surfaces on which the drop maintains a spherical-cap shape during evaporation, as shown in Fig. S1.1 (c) [5,7,8]. However, the roughness features on these surfaces are not electrically accessible; therefore, additional means are needed for electrical detection of biomolecules.

One approach to circumventing the aforementioned integration issue is to design and fabricate asymmetric rough surfaces, such as the periodic array of parallel fins shown in

Fig. S1.1 (d) [9–12]. As discussed extensively in references [12] and [13], there is no energy barrier for fluid transport parallel to the fins, which results in elongation of the droplet in the parallel direction (Fig. S1.1 (d)). On the other hand, facing energy barriers perpendicular to the fins, the contact line pins at the ridge edges, which results in a large hysteresis of the perpendicular contact angle ($\theta_\perp$).
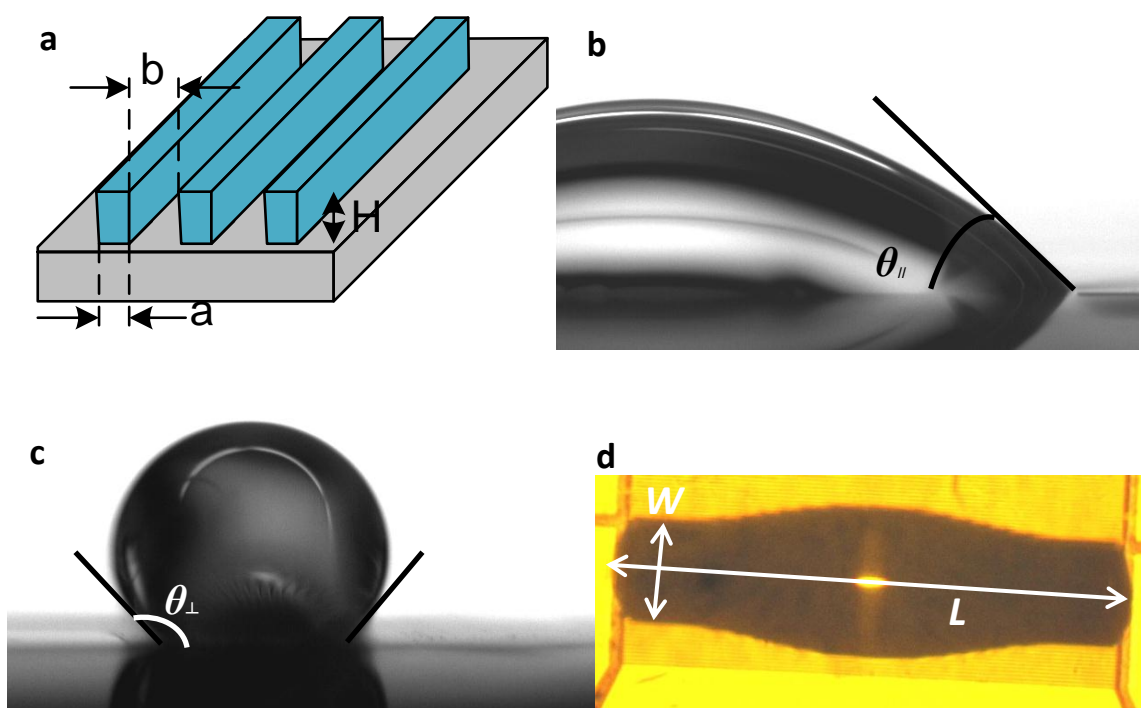

Fig. S1.2 (a) Schematic illustration of the asymmetric electrode array designed to show asymmetric hydrophobic properties. (b) Cross-sectional image of the droplet parallel to the electrodes showing the parallel contact angle ($\theta_\parallel$). (c) Cross-sectional image of droplet in the perpendicular direction for which contact angle ($\theta_\perp$) can be calculated using Eq. S1 (3). (d) An optical top view of the same droplet shown in (b) and (c). The elongation factor used for calculation of $\theta_\perp$ is defined as the ratio of L to W. The pictures in part (b) and (c) were taken using a high-speed camera (RameHart, Model 590).

According to Kusumaatmaja *et al.*, assuming an ellipsoid shape of the droplet footprint, $\theta_\perp$ can be approximated by the following formula [12]:

4

$$\tan\frac{\theta_\perp}{2} = e\tan\frac{\theta_\parallel}{2},\qquad\qquad S1(3)$$

where e is the elongation factor defined as the ratio of the maximum base length of the contact line in the parallel (L) and perpendicular directions (W), and $\theta_\parallel$ is the parallel contact angle of droplet. Immediately after droplet formation, $\theta_\parallel \approx 45\text{-}50°$, as shown in Fig. S1.2 (b).

For a droplet on a symmetric surface (*e.g.* Fig. S1.1 (c)), $e \sim 1$, so that $\theta_\parallel \sim \theta_\perp$. On the other hand, in our case the droplet forms an elongated shape right after deposition, with the final shape characterized by $e \sim 4\text{-}5$ ($L = 4$ mm, $W = 0.8$ mm, see Fig. S1.2 (d)). For $e = 5$ and $\theta_\parallel \approx 45°$, one expects $\theta_\perp \sim 130°$. However, $\theta_\perp$ measured immediately after deposition of the 3 µL droplet on the textured surface is approximately $(146 \pm 6)°$, as depicted in Fig. S1.2 (c). An optical microscope image of the actual droplet elongated on the textured electrode array is shown in Fig. S1.2 (d). The difference between the calculated and measured perpendicular contact angles can be attributed to the secondary nanometer-sized roughness formed on the surfaces of the electroplated nickel electrodes [14] (fabrication details are provided in section S2). The secondary features could also enhance the contact line pinning in the perpendicular direction, which would lead to an effective increase of the perpendicular contact angle. Several researchers have employed such secondary roughness to increase the contact angle and enhance surface hydrophobicity [15,16].

Considering the need to align the liquid contact line with respect to the sensing electrodes during impedance measurement [17], the contact line pinning at the edges of the contact

pads as well as in the perpendicular direction (Fig. S1.2 (d)) helps obtain consistent impedance measurements as the droplet evaporates.

S2 Fabrication of the Nanotextured Superhydrophobic Electrodes

S2-A) Process Flow

The fabrication process of the electrode array is depicted in Fig. S2.1. The SOI wafer (Soitec Co.) was diced and cleaned in Piranha solution (H_2O_2: H_2SO_4, 5:1) for 10 minutes. After rinsing the samples with DI water, it was dried using N_2. For electrical isolation between the electrodes, a 50 nm silicon dioxide (SiO_2) layer was thermally grown on the cleaned sample. A seed-layer, consisting of 20-nm Ti and 90-nm Ni, was deposited using electron-beam (e-beam) evaporation. A 10 μm thick positive photoresist (AZ-9260) was then spin-deposited on the oxidized sample and patterned using standard photolithography to form the mold layer for nickel electroplating. To minimize the fluctuation in current density during electroplating, the sample was cleaned using Reactive Ion Etching (PlasmaLab. RIE) in oxygen plasma to remove any organic residue.

S2-B) Nickel electroplating

Ni electroplating was carried out at temperature of 50°C and at pH of 4 using a mixture of Ni-Sulfamate (25 mL/60 mL), Ni-Bormide (3 mL/60 mL), and Boric Acid (3.7 g/60 mL). The reagents were purchased from Sigma-Aldrich. The DC-current density was maintained at 6 $\mu A/cm^2$ during the electro-deposition. A 8-9 μm thick Ni layer was electroplated on the seed layer selectively based on the photoresist mold. After removing the mold layer by immersing the sample in Acetone/IPA, the Ni layer is removed by a

mixture of H_2O (75 mL):CH_3COOH (25 mL):HNO_3 (25 mL):H_2SO_4 (10 mL), and the Ti

layer is removed by a second solvent mixture of H_2O (20 mL):HF (1 mL).

As shown in Fig. S1.2, there is an inherent nanometer-sized secondary roughness on the

surface of the electroplated electrodes, which increases their hydrophobicity in

comparison with the smooth Ni surface [7,14].

Generally, a very large contact angle ($\geq 150°$) is one of the signatures of a

superhydrophobic surface [7]. The water droplets in this study demonstrate an initial

contact angle of ~$(146 \pm 6)°$, and hence the surface is characterized as being

superhydrophobic. Moreover, using a Veeco Dimension 3100 AFM, the secondary

roughness distribution is characterized by an average height of 300 nm, and a standard

deviation of ~70 nm. This roughness distribution corresponds to a surface with highly

hydrophobic properties [18]. Indeed, the superhydrophobic characteristics of electroplated

nickel films has been noted in [14]. The AFM results and height distribution of the

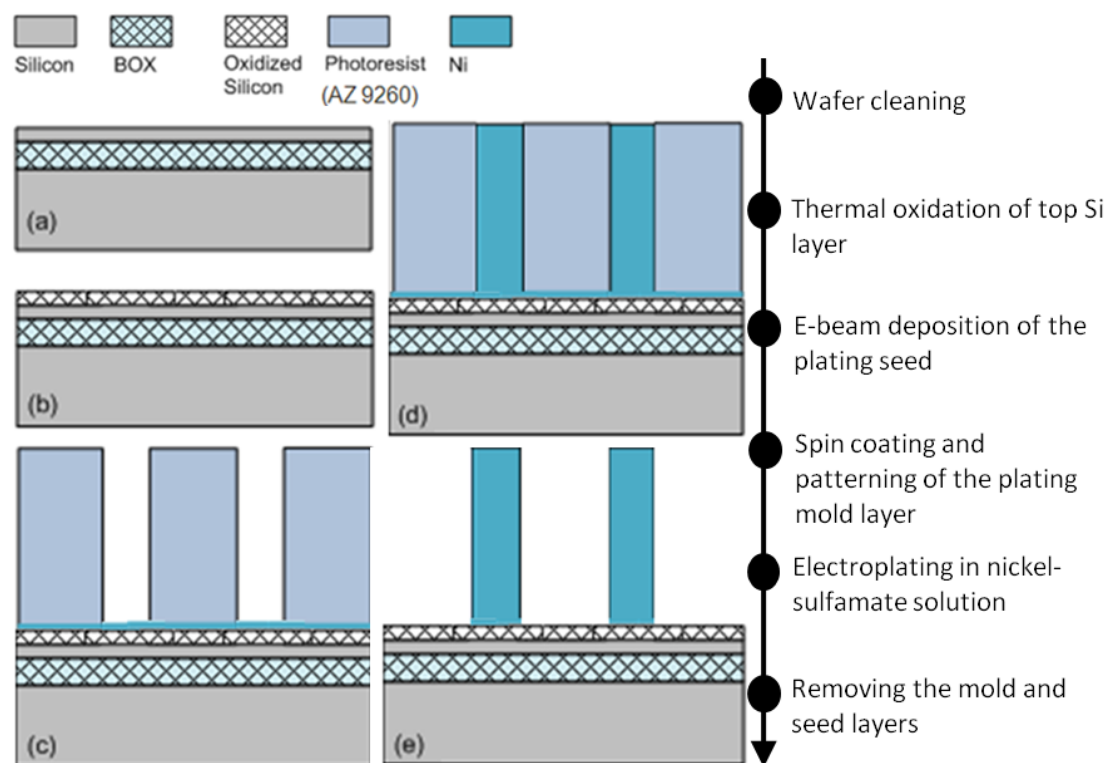nanometer-sized structures are shown in Fig. S2.2 (c).

Fig. S2.1 Schematic illustration of the fabrication process: (a) Cleaning of the substrate SOI wafer, (b) thermal oxidation of the top silicon layer for electrical isolation of individual electrodes, and (c) deposition of the electroplating seed layer (Ti/Ni) in an e-beam evaporation chamber, followed by the mold layer spin coating (AZ9260). The photoresist mold layer is then patterned using standard photolithography. (d) Electrodeposition in nickel-sulfamate solution. (e) Removing the mold layer using acetone, followed by chemical etching of the seed layer to isolate the plated features.
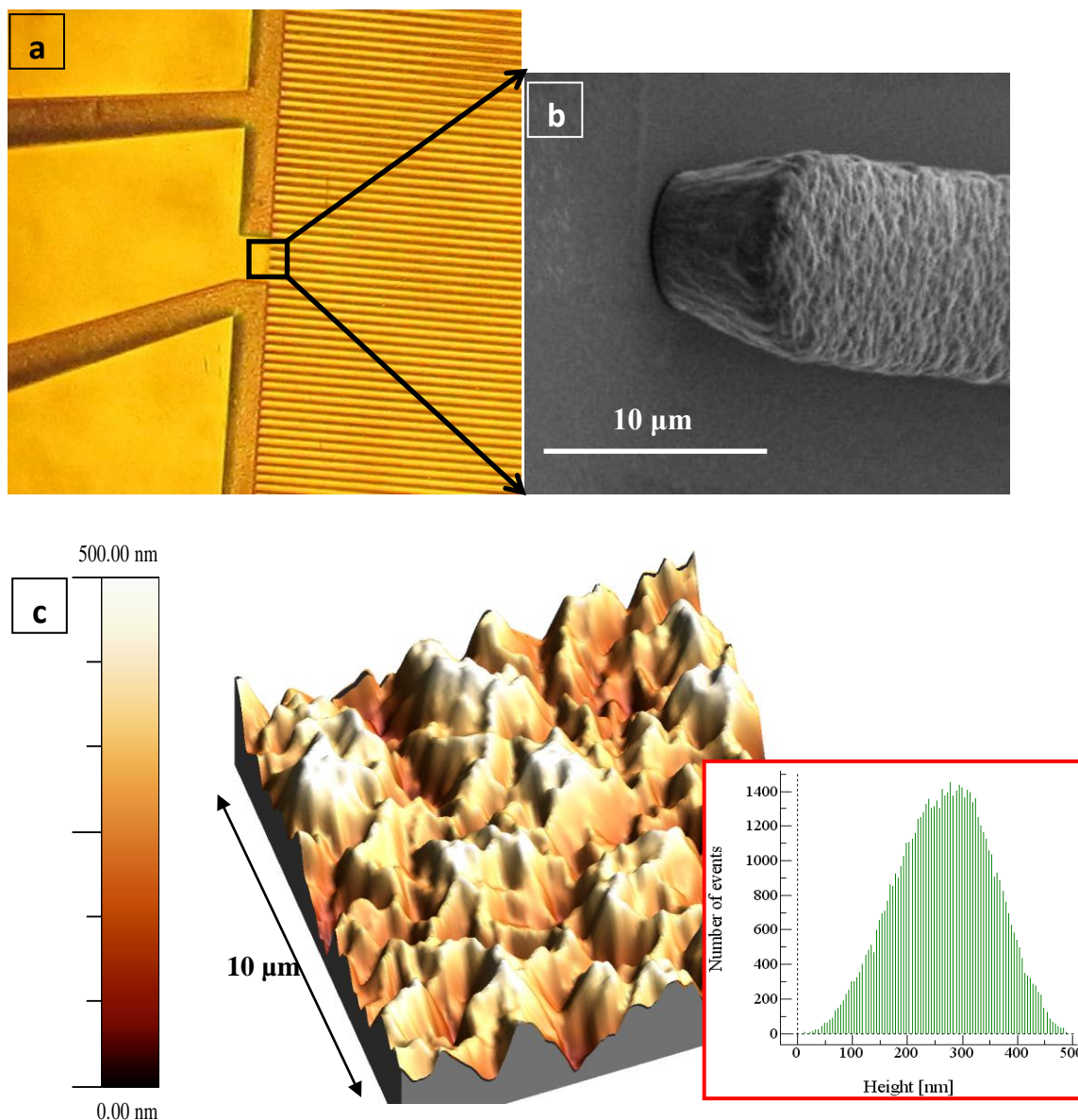
Fig. S2.2 (a) Optical image of the fabricated asymmetric textured electrode array, and (b) an SEM image showing the electroplated Ni fins of height ~8-9 μm. The solid fraction (f_s) for this sample is 1/3. (c) An AFM topograph of the electrodeposited Ni surface depicts the formation of secondary roughness, which increases the hydrophobicity of Ni electrodes. The inset shows the height distribution of the nanometer-sized features. The roughness on the electrodes surface has been formed during the electroplating process.

S3 Dynamics of Droplet Evaporation

S3-A) Experimental Results

Prior to the impedance measurements, a 3 μL droplet is deposited by lowering the pipette tip to the vicinity of the desired region, followed by slow pipetting of the content. When the liquid touches the sensor surface, it spreads along the channels created between adjacent Ni-plated fins and forms the elongated shape shown in Fig. S3.3 (a). In addition, to illustrate the time evolution of the 3 μL droplet during evaporation, a series of images were captured with a high-speed camera (a goniometer, Model 590, RameHart): The perpendicular and parallel cross sections of the evaporating droplet are summarized in Fig. S3.4 and Fig. S3.5, respectively.
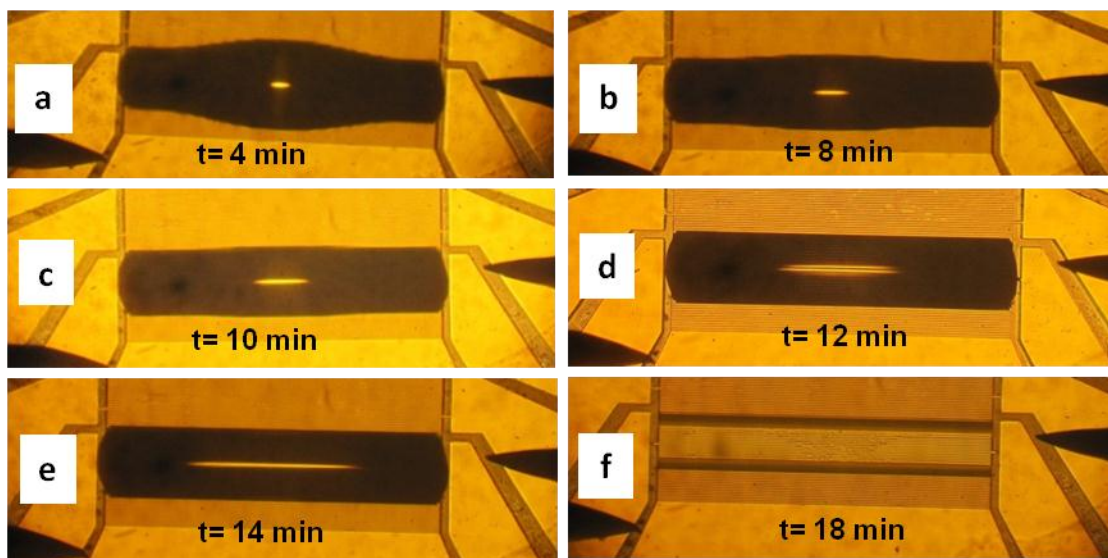

Fig. S3.3 Optical images of a 3 μL droplet evaporating on superhydrophobic nanotextured electrodes after (a) 4 minutes, (b) 8 minutes, (c) 10 minutes, (d) 12 minutes, (e) 14 minutes, and (f) 18 minutes of deposition.
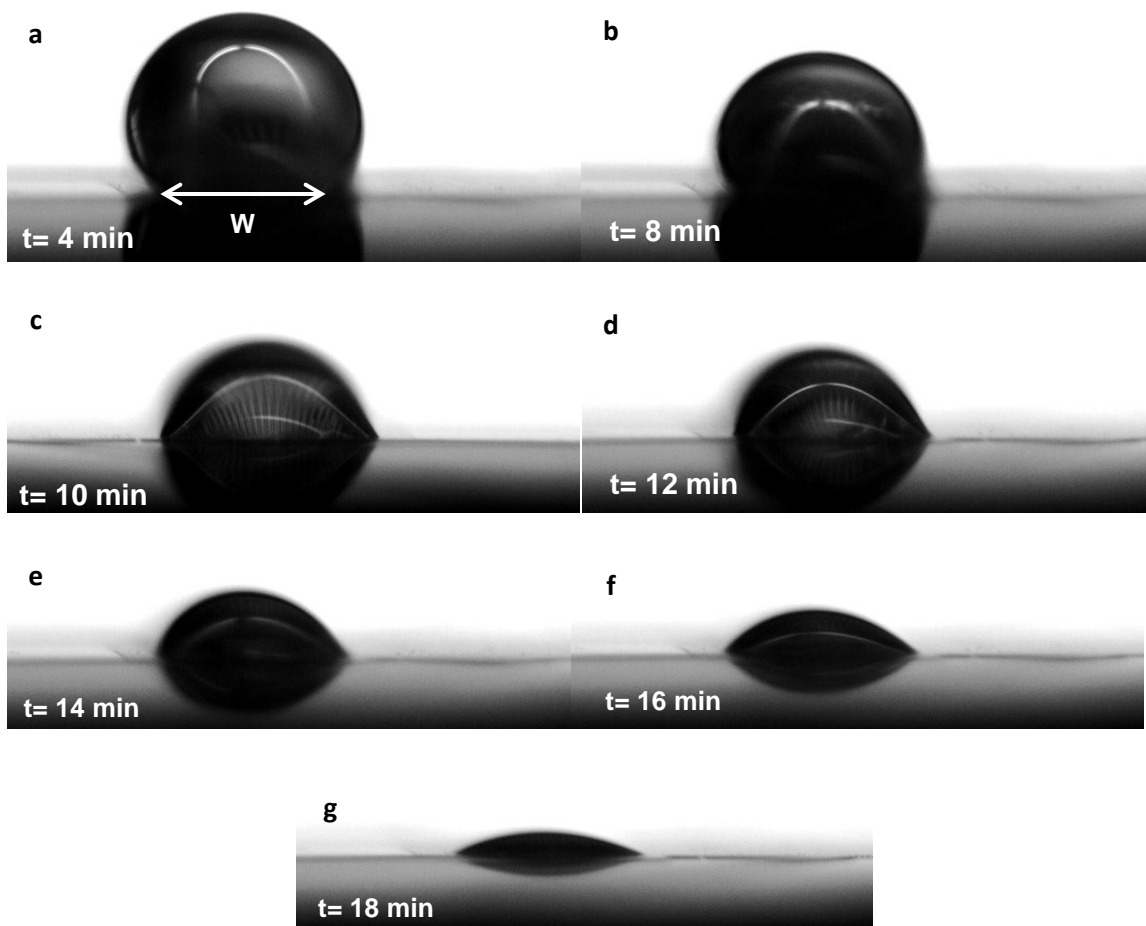
Fig. S3.4 Time evolution of the perpendicular cross section of a 3 μL droplet evaporating on the fabricated Ni-electrode array. It can be seen that the base length in the perpendicular direction (*W*) is time-invariant, showing that the contact line remains constant during evaporation.

Sensor edge

a

t= 4 min

b

t= 8 min

c

t= 10 min

d
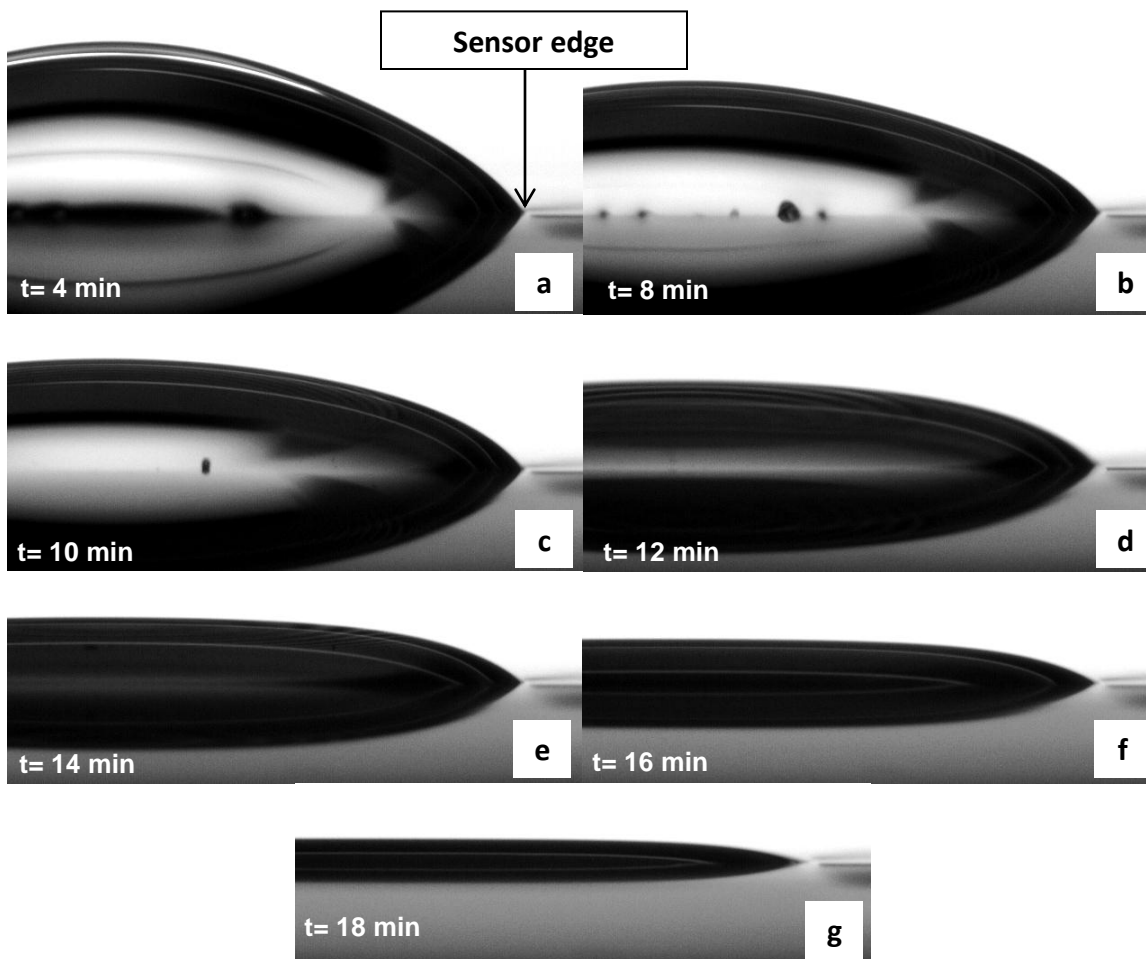
t= 12 min

e

t= 14 min

f

t= 16 min

g

t= 18 min

Fig. S3.5 Time evolution of the parallel cross section of a 3 μL droplet evaporating on the fabricated Ni-electrode array.

We note that the contact lines of the droplet are pinned in both the perpendicular direction (Fig. S3.4) and the parallel direction (Fig. S3.5, an arrow marks the sensor edge).

The time-evolution of the perpendicular and parallel contact angles are plotted in Fig. S3.6 (a) and (b), respectively. These angles are obtained from the images of the cross-section of the droplet at different times, as shown in Fig. S3.4 and Fig. S3.5. These images are also used to calculate of time-evolution of the droplet volume. The symbols reflect the average contact angle of three droplets. The parallel contact angle remains

12

almost constant with time, and the decrease in droplet volume is reflected in the decrease in the perpendicular contact angle. Both the parallel and perpendicular contact angles shown are the average of the right and left contact angles that the droplet forms in contact with the electrodes surface.

According to Fig. S3.6 (b), the droplet volume decreases approximately as $(1 - t/T)^{\frac{3}{2}}$, in which t and T stand for the elapsed time since the droplet is deposited and the total evaporation time of the drop, respectively [19]. Our measurements show that on average T ~20 minutes.
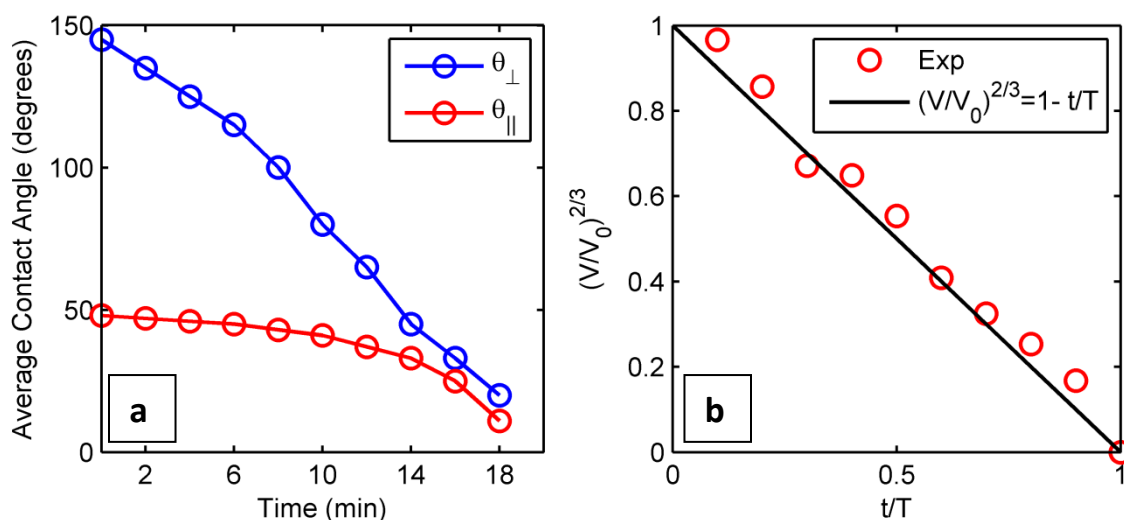

Fig. S3.6 (a) Decrease in the average perpendicular and parallel contact angles of a 3 μL elongated droplet evaporating on the textured electrode array. (b) Time variation of the droplet volume, which decreases with time as $\sim (1 - t/T)^{\frac{3}{2}}$, where t stands for the time since droplet deposition, and T is the total evaporation time (20 minutes).

Finally, to demonstrate the potential of multiplexed and parallel sensing of analytes using a droplet-based platform, we show in Fig. S3.7 an array of three elongated 3 μL droplets

deposited on the sensor surface. Each of these droplets can be addressed individually, and their analyte densities can be probed independently.
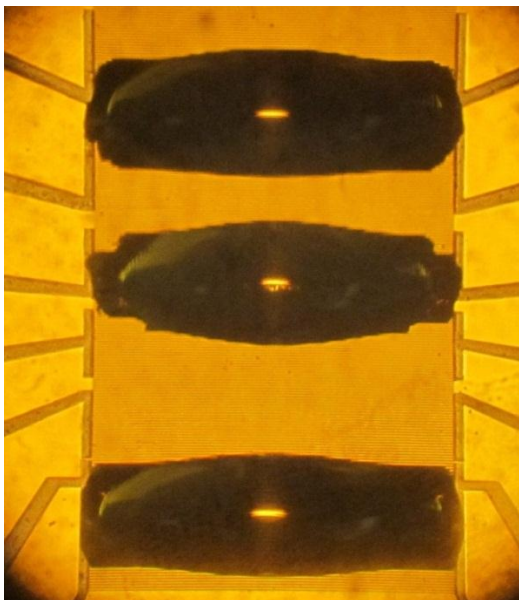

Fig. S3.7 Optical image of an array of droplets on the same sample. This demonstrates the potential of our approach to perform multiple measurements at the same time to increase the data throughput and thereby increase detection accuracy.

S3-B) Simulation of droplet shape using Surface Evolver

In order to determine the shape of the droplet on the fabricated electrode array, we carried out simulations using the public domain software, Surface Evolver [20]. The equilibrium shape of the droplet is a result of minimization of the surface energy. Although our system has grooves and ridges, we consider a simpler surface defined by alternate patches of hydrophobic and hydrophilic regions. Such a mapping reduces computational complexity, while retaining the essential features of the original problem (For a more rigorous analysis see [21]). Our goal here is to understand the qualitative features of the droplet shape, such as elongation of droplet in the direction parallel to the electrode array and the trend that parallel and perpendicular contact angles follow with respect to time.

The simulation is initiated with a drop of given volume resting on a surface with three wettable strips surrounded by dry strips on either side. The aspect ratio of wettable and dry strips was chosen to be $2:1$, so as to mimic $b:a$, the aspect ratio of the electrode fins (Fig. S1.2 (a)) used in the experiments. The surface tensions of the wettable and dry strips are specified to reflect their corresponding contact angles on a flat homogeneous surface. Fig. S3.8 shows the initial and final droplet shapes for a given droplet volume. The initial shape of the droplet is assumed to be a parallelopiped whose length in the y direction is two times that in x direction.
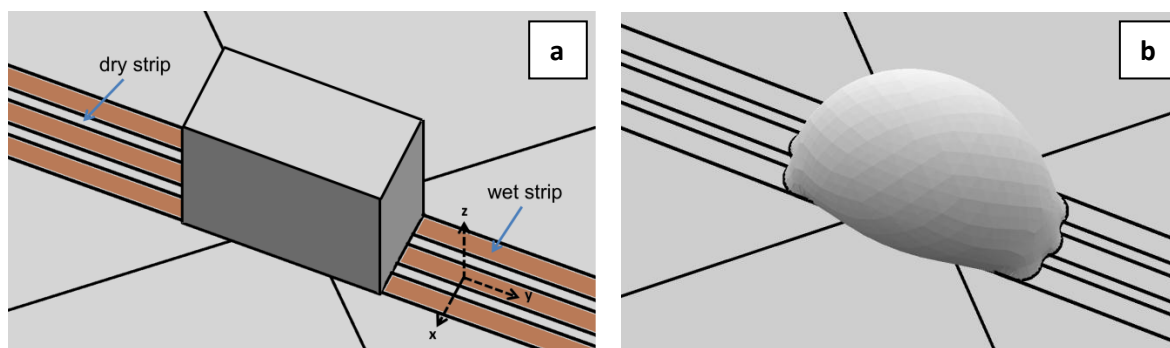

Fig. S3.8: (a) Initial and (b) final shape of a droplet sitting on a surface with three wettable strips surrounded by dry strips.

Fig. 3.8 (b) shows that the computational model correctly anticipates that the droplet elongates more in a direction parallel to the strips compared to the direction perpendicular to the stripes.

The model can compute the equilibrium shape of a droplet of a given volume, but it cannot account for time-dependent evolution of droplet volume through evaporation. To calculate the contact angles as a function of time, we use a quasi-static approach: we first obtain the volume of the droplet for several different instants of time from the

experimental data shown in Fig. S3.6 (b), and then simulate the equilibrium shape (and

the contact angles) of the droplet for volumes associated with specific times. Fig. S3.9

shows the variation of the computed parallel and perpendicular contact angles as a

function of time. Although the simplified model (secondary roughness is ignored, and the

fin-structure of the electrodes is represented by wet/dry stripes) cannot reproduce

quantitatively the experimental results in Fig. S3.6 (a), the simulations correctly

anticipate the key features of the experiments: Both the parallel and perpendicular contact

angles decrease as a function of time and the decrease in perpendicular contact angle is

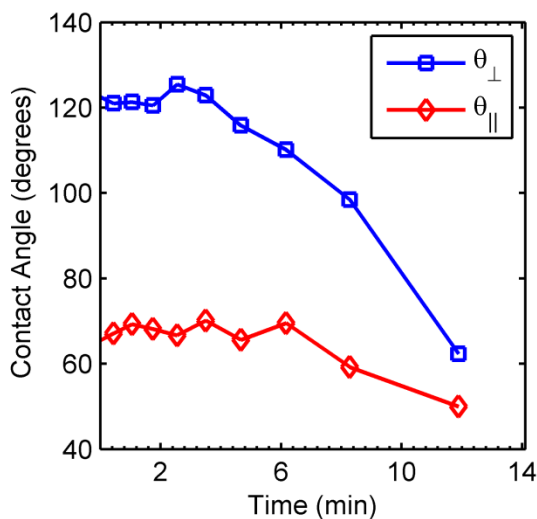steeper than that of the parallel contact angle.

Fig. S3.9 Variation of the computed parallel and perpendicular contact angle for a 3μL droplet as a function of time for the patterned surface shown in Fig. S3.8. These simulation results are in qualitative agreement with the experimentally observed trend as shown in Fig. S3.6 (a).

S4 Preparation of DNA solutions

The originally purchased DNA solutions (Fermentas, Inc.) are 850 bp synthetic molecules in 1xTAE buffer solution (10 mM Tris-EDTA). The DNA molecules were precipitated out of solution using an isopropanol precipitation method and resuspended in DI water. Briefly, the precipitation method involves creating a mixture of the original DNA solution, 7.5 M ammonium acetate, and 100% isopropanol in 1:1:3 volume ratio. This solution was stirred on a table-top vortex mixer. The samples were then loaded into a centrifuge and centrifuged at room temperature for 10 min at 10000 g. The supernatant was then removed and the tube was washed with 1 mL of 100% ethanol by gently inverting the tube several times. The samples were then centrifuged again at 10000 g for 15 min, and the ethanol supernatant pipetted off the DNA pellet. The tube was then left to dry in air for 15 min, so as to remove any leftover ethanol from the tube. Once dry, the DNA molecules were resuspended in nuclease-free DI water and diluted to the desired concentrations.

S5 Impedance Measurement

S5-A) Experimental Results

The impedance measurements are conducted using an LCR meter (HP-4284A). In all the measurements, the signal consisted of a DC bias of 50 mV with an AC level of 10 mV. Plotted in Fig. S5.1 (a) and (b) respectively are the magnitude ($|Z|$) and the phase (θ_Z) of the impedance as a function of frequency, for several DNA concentrations ranging from 1.6 nM to 60 aM. Frequency is swept from 120 Hz to 50 kHz, with a total of 7 frequency

points, and an integrated sweep time of approximately 34 seconds. Fig. S5.1 (a) shows that the ability to discriminate the DNA concentrations through differential impedance reduces with frequency. Consequently, a working frequency of 120 Hz was chosen for the impedance versus time measurements. At lower frequencies (<80-100 Hz), the signal is corrupted by noise of the LCR meter.

For completeness, we plotted in Fig. S5.1 (c) the time-evolution of θ_Z for different DNA concentrations, suggesting that the phase information could be used to distinguish DNA concentrations. Finally, the time-variation of the impedance magnitude of a droplet of DI water ($\left|Z(t)\right|$) is replotted in Fig. S5.1(d), but this time *including* the final jump in the impedance (at $t \sim 20$ min) that indicates complete evaporation of the droplet. Several experiments such as this establish the average evaporation time of an elongated 3 µL droplet to be approximately 20 minutes.
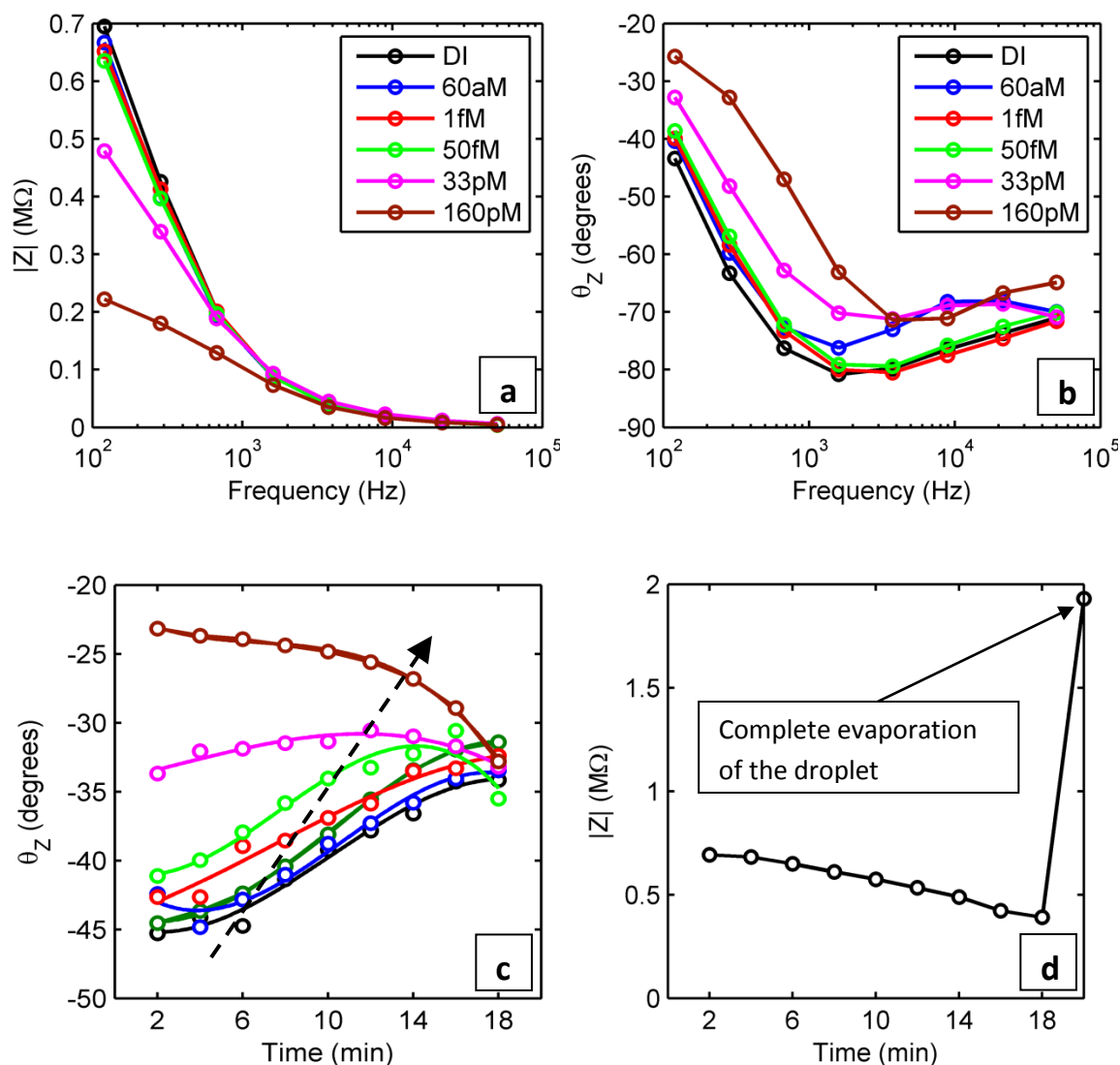
Fig. S5.1 (a) Impedance magnitude versus frequency of a 3 μL droplet at different concentrations measured after 2 minutes of droplet deposition. (b) Impedance phase of the same set of droplets as part (a). (c) Impedance phase of droplets with different DNA concentration as a function of time. The working frequency is 120 Hz. The dashed arrow indicates the concentration increase: DI water (black), 6 aM (dark green), 60 aM (blue), 1 fM (red), 50 fM (light green), 33 pM (magenta), and 160 pM (brown). (d) $|Z|$ vs. time for a 3 μL droplet of DI water. The impedance rise at $t = 20$ min shows that the droplet has completely evaporated after ~ 20 min.

S5-A') The Essential Role of the Nanotextured Surface: Pinning

To demonstrate the essential role of the *nanostructured* electrodes in defining and pinning (self-aligning) the droplet, we fabricated an array of micron-sized 'smooth' Ni electrodes that do not contain secondary, nanostructured roughness. As shown in Fig. S5.2, these smooth electrodes can no longer pin and self-align the droplet. All the droplets had the same initial volume (3 µL) and analyte concentration. Yet, the statistically random contact area and distorted base area of the droplet is reflected in the very large variability of the measured impedance. This point is further demonstrated in Fig. S5.3(a) in which the impedance of three 3 µL droplets deposited on nanotextured and smooth electrodes is monitored and plotted. It is clear from this plot that the impedance of droplets on the smooth electrodes suffers from very large variability and is generally unreliable. This in turn reduces the sensitivity of the detection protocol considerably.

Further, to exhibit the reduced detection resolution of the smooth surface compared to the nanotextured one, the impedance of droplets with two different DNA concentrations is monitored while they evaporate. The impedance results are shown in Fig. S5.3(b). While the impedance difference between 1 pM and 50 pM is detectable on the nanotextured surface, the smooth electrodes on which the droplets spread out, are not able to tell them apart.
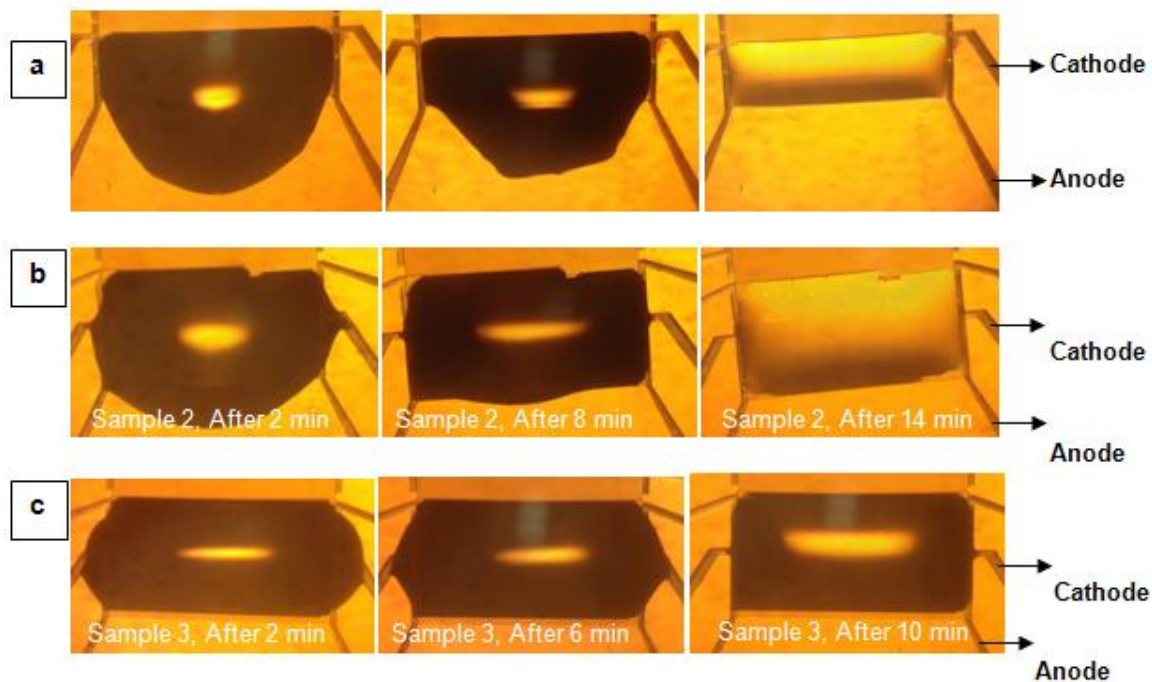
Fig. S5.2: (a)-(c) Time-evolution of three droplets deposited on the smooth electrodes. The droplets spread out and form arbitrary shapes, and as a result, the fluid is not necessarily confined by the cathode and anode (parts b and c).
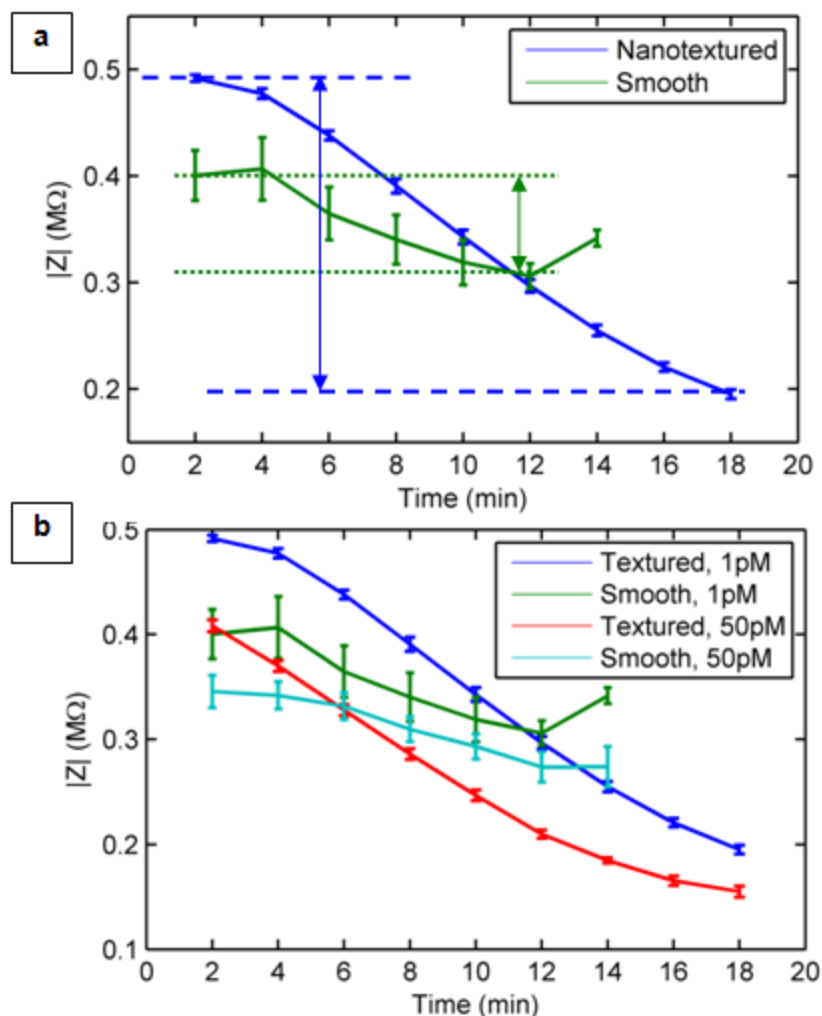
Fig. S5.3: (a) Comparison of impedance sensing of 3 µL droplets of DNA molecules with 1 pM concentration on nanotextured and smooth Ni electrodes. The arrows indicate the total impedance change for each case: Smooth electrode (green), and Nanotextured electrode (blue). (b) Impedance magnitude vs. time for droplets with two different concentrations (1 pM and 50 pM) on smooth and nanotextured electrodes on smooth and nanotextured electrodes. The impedance difference between the two different solution concentrations on the smooth electrodes is less and has a large variation compared to the sensor with nanotextured electrodes. In both plots, the frequency is 120 Hz.

S5-B) Simulation of Impedance Characteristics

To understand the physics underlying the change in impedance as a function of DNA concentration and evaporation time, we used a compact modeling approach as follows.

Fig. S5.4 shows the compact model used to characterize the intrinsic parameters of the solution and the caption defines the various elements of the impedance network. The net impedance of the circuit is given by $Z = R_{electrode} + \left(Z_{sub} \| Z_{droplet} \right)$, where

$$Z_{droplet} = 2Z_{dl} + \frac{R_{sol}}{1 + j\omega C_{sol} R_{sol}}$$ is the impedance of the droplet.
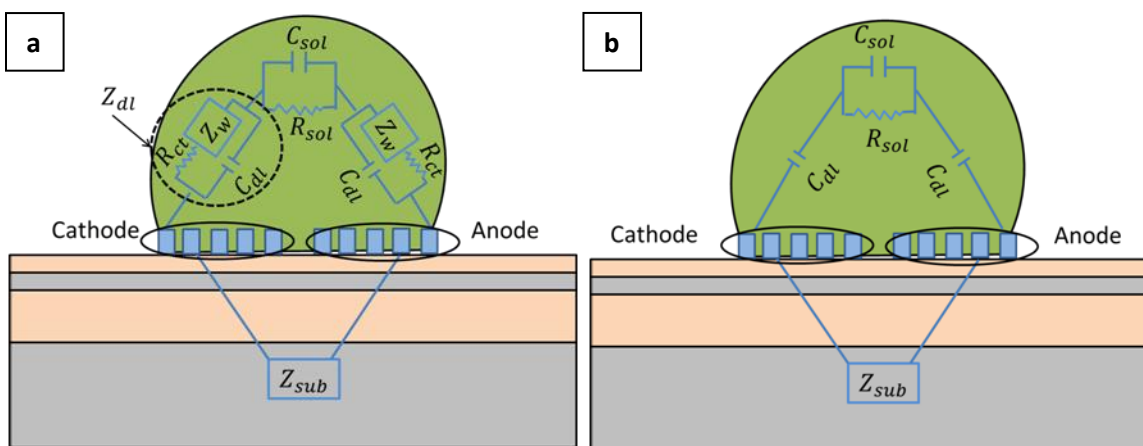

Fig. S5.4: (a) Compact circuit model for impedance measurements: Z_{sub} represents the impedance due to parasitic capacitance from the oxide and the parasitic resistance due to the substrate underneath; R_{sol} represents the solution resistance, C_{sol} the dielectric capacitance of the solution, Z_{dl} the double layer impedance at the electrode electrolyte interface, and $R_{electrode}$ the resistance of the electrodes. Z_{dl} is composed of a parallel combination of the double layer capacitance (C_{dl}) and the charge-transfer resistance (R_{ct}) of the electrode-electrolyte interface. Z_W is the Warburg impedance. (b) Simplified circuit model for impedance measurement.

The following procedure was followed for determination of the parameters of the compact model (summarized in Supplementary Table S5.1):

1. *Parasitic Electrode Resistance:* $R_{electrode}$ was extracted from the DC I-V measurements on the electrodes.

2. *Parasitic Substrate Impedance*: Next, the (parasitic) impedance associated with the substrate (Z_{sub}) was obtained from the frequency-dependent impedance measurements between anode and cathode in the absence of droplet, see Fig. S5.5. For a highly sensitive biosensor, the parasitic impedance Z_{sub} should be as high as possible, therefore, we used a low frequency of 120 Hz. In this case we found that $|Z_{sub}| = 2$ MΩ.
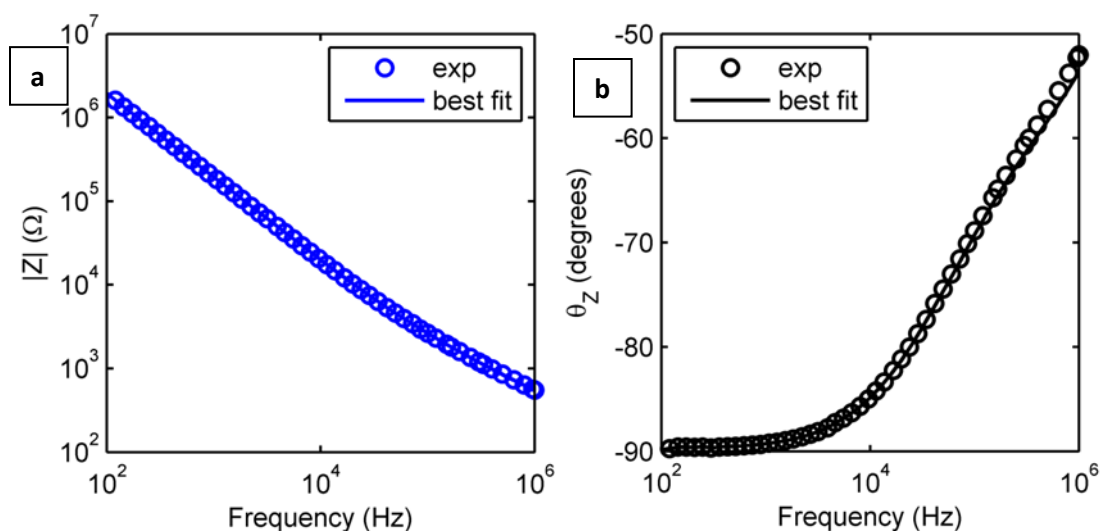

Fig. S5.5: Experimental data for (a) magnitude and (b) phase of the parasitic impedance as a function of frequency.

3. *Droplet Warburg Impedance*: On the other hand, 120 Hz is considered sufficiently high to ensure electrokinetic diffusion is suppressed and the Warburg impedance (Z_W) can be ignored [22].
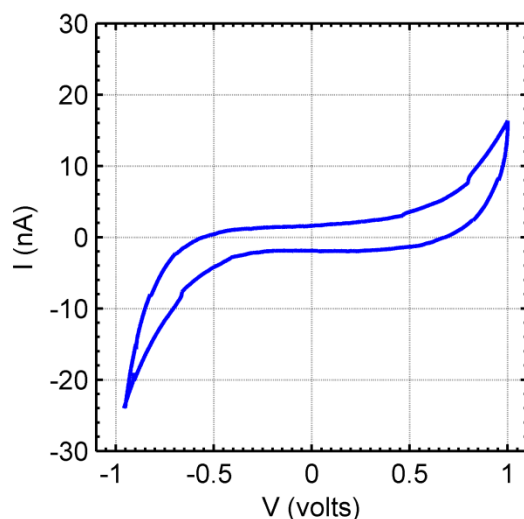
Fig. S5.6: I-V measurement for extraction of R_{ct}. The applied voltage was swept at a rate of 10 mV/s.

4. *Droplet Charge-Transfer Resistance*: Since we are working in a non-faradaic regime and DI water serves as the buffer solution for the DNA molecules, one may assume that the charge transfer resistance (R_{ct}) is very high, *i.e.*, there is essentially no charge transfer between the electrolyte and the electrode surface. To validate this assumption, we measure the I-V characteristics of a reference droplet of DI water with a ramp rate of $10 \, mV/s$, see Fig. S5.6. Once the parasitic resistances are accounted for, the DC equivalent circuit of the droplet (see Fig. S5.4) involves a series connection of R_{ct} and R_{sol} (*i.e.*, $R_{tot} \sim R_{sol} + 2R_{ct}$). R_{tot} was extracted from the slope of the I-V curves between -0.5V to 0.5 V. We will show below that $R_{sol} \ll R_{ct}$, therefore, $R_{ct} \sim R_{tot}/2$. Using this approach, we found that R_{ct} of a 3 μL DI droplet is ~1.4 GΩ. This very large resistance can be safely ignored for subsequent analysis of the experimental data.

25

Solution Impedances of a Droplet: With Z_w, Z_{sub} and R_{ct} specified, we then matched the experimental impedance data for DI water (Fig. S5.7) to obtain the remaining parameters C_{sol} , R_{sol} and C_{dl} for DI water. Note that C_{sol} is exclusively dependent on the shape/volume of the droplet and the permittivity of the medium. In the following analysis, we will assume that permittivity of the solution remains unchanged even when DNA molecules are introduced in DI water. The approximation is justified for the very low DNA concentration ($<$ 1 nM) used in our experiments. This implies that we can assume C_{sol} to be independent of DNA concentration. We attribute the change in impedance for different DNA concentration to the change in solution resistance R_{sol} and double layer capacitance, C_{dl}.

With all other circuit parameters already determined (Table S5.1) and using Eq. S5 (1), S5 (2), and S5 (3) given in Table S5.2, R_{sol} and C_{dl} were extracted from the experimentally obtained impedance (Z) for each DNA concentration and at $f = 120$ Hz. Since R_{sol} and C_{dl} are frequency independent, the same pair of values should also explain, with no further adjustment, the measured frequency characteristics of the impedance ($Z(f)$) over the entire frequency range. Fig. S5.7 (for DI water) and Fig S5.8 (for two different DNA concentrations) demonstrate that this is indeed the case, and therefore, the parameters obtained from the compact model are self-consistent and physically justified.
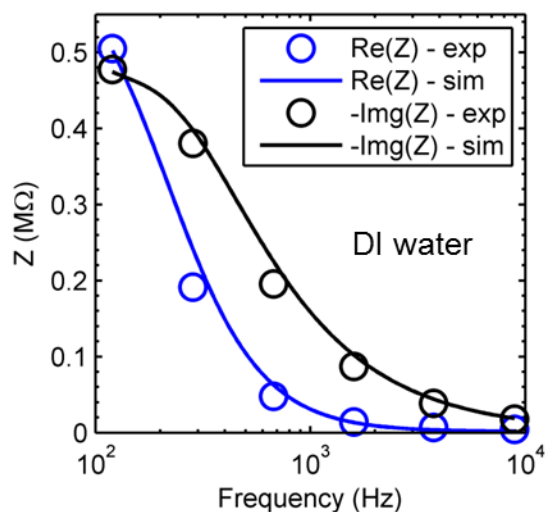
Fig. S5.7: A good match between the experimental and simulation results for the real and imaginary parts of the total impedance (Z) of DI water as a function of frequency.
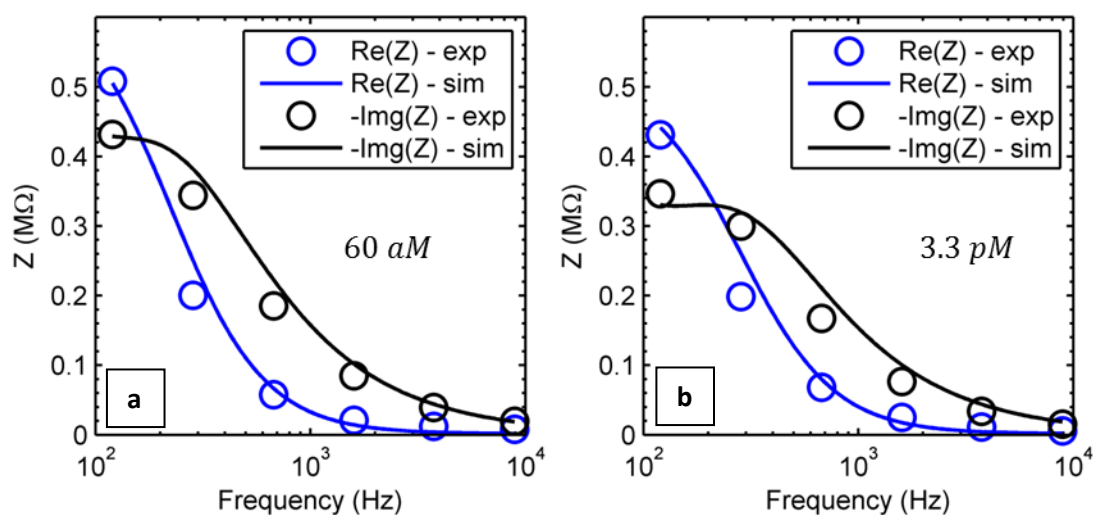

Fig. S5.8: Real and imaginary parts of the impedance for two different DNA concentrations: (a) 60 aM (b) and 3.3 pM. There is close agreement between the experimental and simulation results in both figures.

Supplementary Table S5.1: List of different parameters and the method of extraction.

Parameter	Value	Method of Extraction
$R_{electrode}$	$\sim 20\ \Omega$	DC I-V measurements without droplet
R_{ct}	$1.4 \times 10^9\ \Omega$	I-V measurements on a droplet of DI water
Z_{sub}	$10^2 - 10^6\ \Omega$	Impedance measurements without droplet
C_{sol}	0.12 nF	Curve-fitting of impedance for DI water
$C_{dl}{}^{23}$	$10 - 70$ nF	Curve-fitting of impedance for each DNA concentration
R_{sol}	$10^5 - 10^6\ \Omega$	Curve-fitting of impedance for each DNA concentration

Supplementary Table S5.2: Model Equations

$$Z = R_{electrode} + \frac{Z_{sub} Z_{droplet}}{Z_{sub} + Z_{droplet}}$$	Eq. S5 (1)
$$Z_{droplet} = 2Z_{dl} + \frac{R_{sol}}{1 + j\omega C_{sol} R_{sol}}$$	Eq. S5 (2)
$$Z_{dl} = \frac{R_{ct}}{1 + j\omega C_{dl} R_{ct}}$$	Eq. S5 (3)

S5-C) Specificity of the Evaporation-Enhanced Impedance Sensing

We have conducted two sets of experiments to experimentally demonstrate the specificity of the proposed approach in identifying the length and state of DNA molecules (ssDNA vs. dsDNA).

Length-Dependent Differentiation of DNA molecules

Studies on the electrical properties of DNA molecules in aqueous solution show that because of the existence of mobile charges in and around the DNA, a dipole moment is induced in DNA when the solution is under an alternating electrical field [24-26]. This results in an effective increase in the charge density (decrease in the impedance magnitude) with DNA length (or concentration) [24,25].

To show the capability of our approach in differentiation of different DNA lengths, the impedance of two sets of droplets containing 50 bp and 500 bp dsDNA molecules at a frequency of 120 Hz is monitored while they evaporate (see Fig. S5.9). Based on these plots, the ability of the proposed non-Faradaic impedance sensing in specifically identifying different DNA lengths is validated.
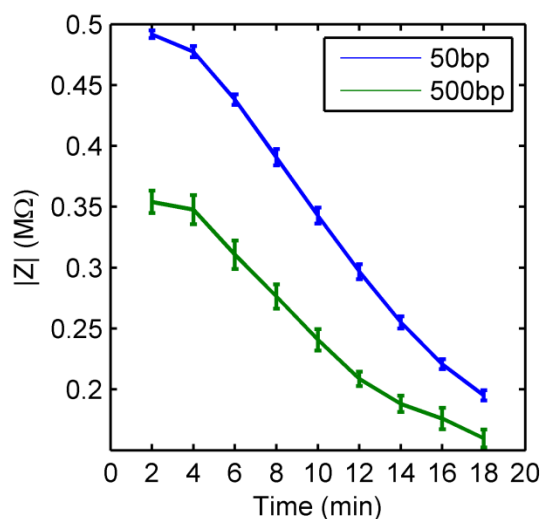
Fig. S5.9: Impedance magnitude vs. time for two different lengths at 120 Hz: 50 bp and 500 bp dsDNA molecules at a concentration of 1 pM.

Differentiation of ssDNA from dsDNA

To demonstrate the capability of the proposed impedance sensing platform in identifying the DNA state in solution, two sets of solutions were prepared: 500 bp ssDNA (non-hybridized strands) and 500 bp dsDNA (hybridized strands). 3 μL droplets of each solution were deposited on the nanotextured electrode array and their impedance was monitored as the droplets were evaporating. The impedance measurement results summarized in Fig. S5.10(a) imply that solutions with ssDNA molecules have lower impedance magnitude (higher conductance) compared to those with dsDNA. This is consistent with the hypothesis that 'trapped' counterions, which are schematically shown in Fig. S5.10(b), are released in the transition from dsDNA to ssDNA states and as a result the solution conductivity increases [26-28].
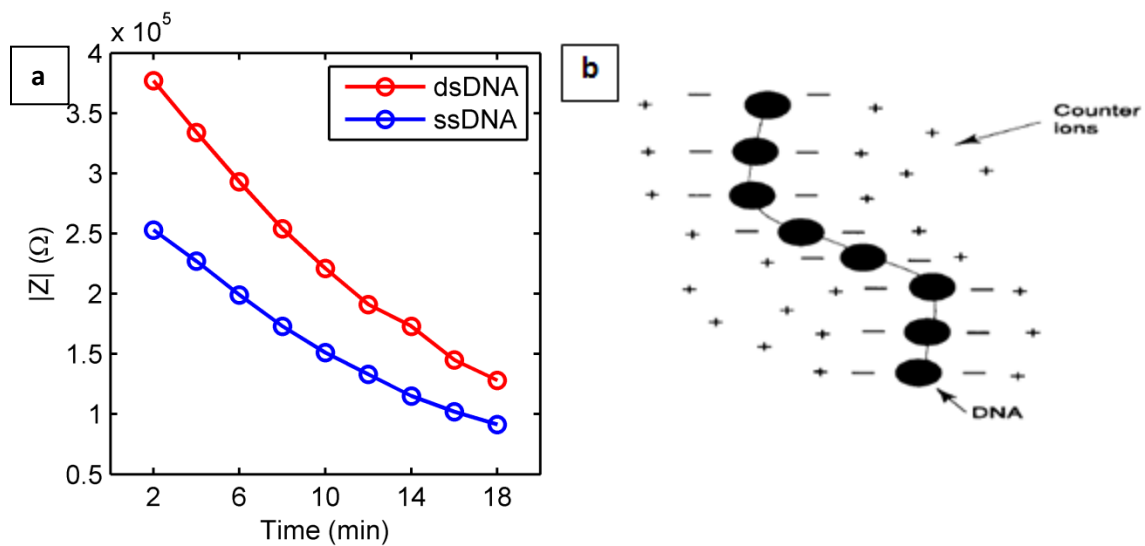
Fig. S5.10: (a) Impedance magnitude as a function of time for 3 μL droplets containing dsDNA vs. ssDNA with length of 500 bp at concentration of 1 pM. The applied frequency is 120 Hz. (b) A graphical representation of counterions around a DNA molecule. [26]

References

1.   O. Bliznyuk, Ph.D. Thesis, University of Twente, 2011.

2.   B. He, N. A. Patankar, and J. Lee, *Langmuir*, 2003, **19**, 4999–5003.

3.   G. McHale, S. Aqil, N. J. Shirtcliffe, M. I. Newton, and H. Y. Erbil, *Langmuir*, 2005, **21**, 11053–11060.

4.   D. Quere, A. Lafuma, and J. Bico, *Nanotechnology*, 2003, **14**, 1109–1112.

5.   A. Dupuis and J. M. Yeomans, *Langmuir*, 2005, **21**, 2624–2629.

6.   C. Neinhuis and W. Barthlott, *Ann. Bot.*, 1997, **79**, 667–677.

7.   S. Dash, N. Kumari, and S. V. Garimella, *J. Micromech. Microeng.*, 2011, **21**, 105012.

8.   A. Nakajima, *NPG Asia Mater.*, 2011, **3**, 49–56.

9.   R. David and a. W. Neumann, *Colloids Surf. A*, 2012, **399**, 41–45.

10.   D. Xia, X. He, Y.-B. Jiang, G. P. Lopez, and S. R. J. Brueck, *Langmuir*, 2010, **26**, 2700–2706.

11.   L. Liu, A. M. Jacobi, and D. Chvedov, *J. Micromech. Microeng.*, 2009, **19**, 035026.

12.   H. Kusumaatmaja, R. Vrancken, C. W. Bastiaansen, and J. M. Yeomans, *Langmuir*, 2008, **24**, 7299–7308.

13.   O. Bliznyuk, V. Veligura, E. Kooij, H. Zandvliet, and B. Poelsema, *Phys. Rev. E*, 2011, **83**, 041607.

14.   T. Hang, A. Hu, H. Ling, M. Li, and D. Mao, *Appl. Surf. Sci.*, 2010, **256**, 2400–2404.

15.   W. Ming, D. Wu, R. Benthem, and G. With, *Nano Lett.*, 2005, **5**, 2298–301.

16.   B. Bhushan, K. Koch, and Y. C. Jung, *Ultramicroscopy*, 2009, **109**, 1029–34.

17.   P. Mirtaheri, S. Grimnes, and O. G. Martinsen, *IEEE Trans. Biomed. Eng.*, 2005, **52**, 2093–2099.

18.   B. Bhushan, Y. Wang, and A. Maali, *Langmuir*, 2009, **25**, 8117–8121.

19.   S. Dash and S. V. Garimella, *Langmuir*, DOI: 10.1021/la402784c.

20.   K. A. Brakke, Surface Evolver.

21.   Y. Chen, B. He, J. Lee, and N. Patankar, *J. Colloid Interface Sci.*, 2005, **281**, 458–64.

22.   D. Berdat, A. Marin, F. Herrera, and M. Gijs, *Sens. Actuators, B*, 2006, **118**, 53–59.

23.   A. J. Bard and L. R. Faulkner, J. Wiley, New York, 2nd edn., 2001, vol. 677, p. 833.

24.   Y.-S. Liu, P. P. Banada, S. Bhattacharya, A. K. Bhunia, and R. Bashir, *App. Phys. Lett.*, 2008, **92**, 143902.

25.   M. Hanss, *Biopolymers*, 1973, **12**, 2151

26.   J. Baker-Jarvis, C. A. Jones, and B. Riddle, *NIST Tech. Note*, 1998, 1509.

27.   A. G. Georgakilas, K. S. Haveles, E. G. Sideris, *IEEE Trans. on Dielectr. and Electr. Insul.*, 1998, **5**, 26-32.

28.   T. Vuletic, S. Dolanski Babic, D. Grgicin, D. Aumiler, J. Radler, F. Livolant, and S. Tomic, *Phys. Rev. E*, 2011, **83**, 041803.